




Article

The Role of HNO₂ in the Generation of Plasma-Activated Water by Air Transient Spark Discharge

Mário Janda * , Karol Hensel , Peter Tóth, Mostafa E. Hassan  and Zdenko Machala 

Faculty of Mathematics, Physics and Informatics, Comenius University Mlynská Dolina, 84248 Bratislava, Slovakia; karol.hensel@fmph.uniba.sk (K.H.); toth169@uniba.sk (P.T.); mostafa.hassan@fmph.uniba.sk (M.E.H.); zdenko.machala@fmph.uniba.sk (Z.M.)

* Correspondence: mario.janda@fmph.uniba.sk

Abstract: Transient spark (TS), a DC-driven self-pulsing discharge generating a highly reactive atmospheric pressure air plasma, was employed as a rich source of NO_x. In dry air, TS generates high concentrations of NO and NO₂, increasing approximately linearly with increasing input energy density (E_d), reaching 1200 and 180 ppm of NO and NO₂, at $E_d = 400$ J/L, respectively. In humid air, the concentration of NO₂ decreased down to 120 ppm in favor of HNO₂ that reached approximately 100 ppm at $E_d = 400$ J/L. The advantage of TS is its capability of simultaneous generation of the plasma and the formation of microdroplets by the electrospray (ES) of water directly inside the discharge zone. The TS discharge can thus efficiently generate plasma-activated water (PAW) with high concentration of H₂O₂[−](aq), NO₂[−](aq) and NO₃[−](aq), because water microdroplets significantly increase the plasma-liquid interaction interface. This enables a fast transfer of species such as NO, NO₂, HNO₂ from the gas into water. In this study, we compare TS with water ES in a one stage system and TS operated in dry or humid air followed by water ES in a two-stage system, and show that gaseous HNO₂, rather than NO or NO₂, plays a major role in the formation of NO₂[−](aq) in PAW that reached the concentration up to 2.7 mM.

Keywords: non-thermal plasma; transient spark; electrospray; plasma-activated water; nitrous acid; nitrites



Citation: Janda, M.; Hensel, K.; Tóth, P.; Hassan, M.E.; Machala, Z. The Role of HNO₂ in the Generation of Plasma-Activated Water by Air Transient Spark Discharge. *Appl. Sci.* **2021**, *11*, 7053. <https://doi.org/10.3390/app11157053>

Academic Editor: Andrei Vasile Nastuta

Received: 8 July 2021
Accepted: 28 July 2021
Published: 30 July 2021

Publisher's Note: MDPI stays neutral with regard to jurisdictional claims in published maps and institutional affiliations.



Copyright: © 2021 by the authors. Licensee MDPI, Basel, Switzerland. This article is an open access article distributed under the terms and conditions of the Creative Commons Attribution (CC BY) license (<https://creativecommons.org/licenses/by/4.0/>).

1. Introduction

Highly reactive non-thermal (cold) plasmas (NTP) in atmospheric air can be generated by various electrical discharges. Their high chemical activity is due to the presence of high energy electrons. The NTP are therefore very commonly used in various environmental, surface processing, or biomedical applications [1–3]. The research interest focused on the cold plasma applications in biology and medicine has dramatically grown during the last decades, because NTP can efficiently inactivate bacteria and other dangerous microbes and induce interesting therapeutic effects, e.g., against cancer cells [4,5].

There are several biocidal agents provided by non-thermal plasma treatments: UV radiation, ions, and reactive neutral species [6–8]. The role of individual agent can vary depending on the used plasma source, input energy density, or gaseous environment. The reactive oxygen and nitrogen species (RONS) were demonstrated as the key biocidal agents produced in the transient spark (TS) air discharge extensively studied in our group [9]. We previously reported that the dominant gaseous products in the air treated by TS were nitric oxide (NO) and nitrogen dioxide (NO₂) [10].

Biomedical applications of NTP often lead to the interaction of plasmas with liquid media (e.g., water). The generation of NTP in contact with water has therefore become a hot topic over the last few years [11]. Transport of active species from the plasma (gas phase) into the liquid phase leads to the production of so-called plasma-activated water (PAW), with various potential applications in medicine (e.g., wound healing or inactivation of cancer cells) or in agriculture (e.g., seed germination and plant growth

promotion, pest control) [12–16]. With PAW, the biocidal effects of plasma can be indirectly applied in cases where a direct plasma treatment is not possible.

The composition of PAW and thus also its potential application varies with the used plasma source and working gas [15,17]. The liquid phase RONS in PAW include long-lived species: ozone ($O_{3(aq)}$), hydrogen peroxide ($H_2O_{2(aq)}$), nitrites ($NO_2^-(aq)$), or nitrates ($NO_3^-(aq)$), besides short-lived species that are challenging for diagnostics: hydroxyl OH, peroxy HO_2 radicals, atomic O, N and H, singlet molecular O_2 ($^1\Delta$), superoxide anion O_2^- and other ions. Transport of reactive species from gas to water is the primary source of the liquid RONS, but the composition of liquid RONS does not perfectly mirror the concentrations of gaseous RONS. First, the concentration of liquid phase RONS depends on the solubility of their gas phase counterparts. Second, the composition of PAW is influenced by a rich set of the subsequent chemical reactions in the liquid phase [18,19].

The highest achievable (saturated) concentration of species in liquid phase c_i^{satur} is determined by Henry's law:

$$c_i^{satur} = k_H^i p_i \quad (1)$$

Here p_i is partial pressure and k_H^i is the Henry's law coefficient of i -species. For instance, H_2O_2 (with $k_H = 108,000 \text{ mol}\cdot\text{kg}^{-1} \text{ atm}^{-1}$ at 298.15 K [20]) is much more soluble than many other gas phase RONS, having k_H by seven orders of magnitude higher than O_3 and NO_2 , and by eight orders of magnitude higher than NO. The high solubility of H_2O_2 leads to the depletion of its gas phase concentration near the liquid interface [21,22]. The highest achievable concentration of $H_2O_{2(aq)}$ in the liquid phase is thus limited by the number of available H_2O_2 molecules in the gas phase. On the other hand, for weakly soluble molecules, such as O_3 , the assumption of the constant concentration and partial pressure in the gas phase is valid. Here, the saturated concentration in the liquid phase could be achieved without a noticeable decrease of O_3 concentration in the gas phase. In plasma-liquid interactions, the situation is much more complicated, because solubility determined by Henry's law coefficient is valid for systems in thermodynamic equilibrium. This is certainly not the case of NTP interacting with water. Electric fields, temperature gradients, electrohydrodynamic spray of liquids, charging of water droplets, ionic wind, chemical reactions among various species, and other phenomena make solvation of reactive species from NTP to water very complicated process that is still not completely understood [11,21].

The plasma-liquid interface surface area is a key parameter maximizing the contact between the plasma and the treated water solution, thus determining the obtained plasma chemical effects [23]. The transformation of bulk water into fine droplets results in an increase of this interfacial surface area and thus accelerates the transport of reactive plasma species into the water. The electrohydrodynamic spray of liquids, here simply called electrospray (ES), is a simple process to produce microdroplets from bulk liquid by a strong electric field. Despite the pioneering experimental studies describing several ES modes were conducted more than a century ago [24,25], due to a high application potential of ES in many areas [26–31], the research of ES continues [32–34], and several reviews were published recently focused on different aspects of ES [35–37].

The idea of using ES microdroplets to increase plasma-water interface area has been adopted by several research groups [21,38–40], as well as in our previous works [15,41]. For instance, TS was also used to prepare PAW by the electrospray of fine aerosol droplets directly through the active plasma zone, which resulted in a very efficient transfer of gaseous RONS into water. The PAW generated by TS contains besides $H_2O_{2(aq)}$ high concentration of $NO_2^-(aq)$ and $NO_3^-(aq)$ [15]. This was attributed to the fact that the dominant gas phase species in air TS are NO and NO_2 .

In this paper we focus on the possible role of gas phase nitrous acid (HNO_2) on the PAW generation by TS. Even with much lower gas phase concentration than NO_2 and NO, HNO_2 may influence PAW generation significantly since the k_H of HNO_2 ($50 \text{ mol}\cdot\text{kg}^{-1} \text{ atm}^{-1}$ at 298.15 K [42]) is four and five orders of magnitude higher than k_H of NO_2 ($0.007 \text{ mol}\cdot\text{kg}^{-1} \text{ atm}^{-1}$ at 295 K [43]) and NO ($0.0018 \text{ mol}\cdot\text{kg}^{-1} \text{ atm}^{-1}$ at 298.15 K [44]),

respectively. In our previous work, we were able to detect small amounts of HNO_2 in the gas phase using the Fourier transform infrared (FT-IR) spectroscopic technique [45]. A new diagnostic technique (direct UV-Vis absorption spectroscopy) allowed us to perform a more precise HNO_2 diagnosis in the TS-treated air when installed much closer to the plasma reactor. Moreover, the experiments where PAW is prepared by the direct ES of microdroplets directly through the discharge zone in a common one-stage system are compared to the experiment with a two-stage system, with one reactor for the TS air treatment followed by the ES of water microdroplets in the second reactor.

2. Materials and Methods

Several types of experiments were performed in a one-stage system (1SS) with a single reactor (Figure 1), or in two-stage system (2SS) with two reactors in series (Figure 2). In 1SS, the single reactor enables a simultaneous generation of TS with a direct ES of water. This reactor can be also used for generation of TS without ES, or vice-versa, for generation of ES without TS. In 2SS, the gas is treated by TS inside the first reactor, and subsequently passed into the second reactor with water electrospayed on the microdroplets. In 2SS, the second reactor is the same as the single reactor used in 1SS (Figure 2).

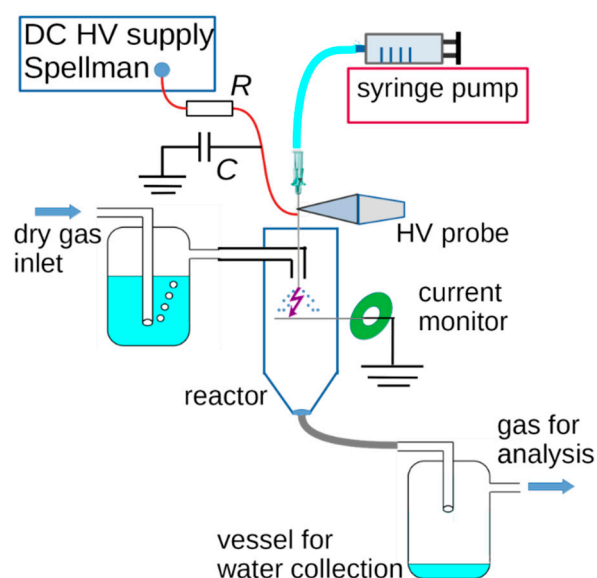


Figure 1. Simplified schematic of the experimental setup of one-stage system (1SS), with a single reactor enabling simultaneous TS and ES generation; R—resistor, C—capacitor, HV—high voltage.

The treated air was either dry synthetic air (99.999% purity, Messer Tatragas, Bratislava, Slovakia), or humidified synthetic air. In addition, dry and humidified O_2 (99.95% purity, Linde Gas, Bratislava, Slovakia) were used in two comparative experiments. In order to moisturize the gas, the dry air was bubbled through a bubbler filled with deionised (DI) water (with conductivity $< 3 \mu\text{S}/\text{cm}$). Typically, the relative humidity around 94–96% was achieved, verified by humidity sensor. The gas flow rate 1.1 L/min was constant in all experiments, controlled by rotameters Aalborg. We also performed additional comparative experiments in 1SS focused on NO and NO_2 solvation to ES water microdroplets without discharge. For this purpose, as well as for calibration of spectrometers, two special pressure tanks with calibration gases were used: one with 2000 ppm of NO in N_2 , the second one with 1000 ppm of NO_2 in synthetic air. Lower concentration of NO and NO_2 was achieved by mixing of gases from these bottles with N_2 or synthetic air, respectively. More specific description of the used discharge and individual components of our experimental setups follow.

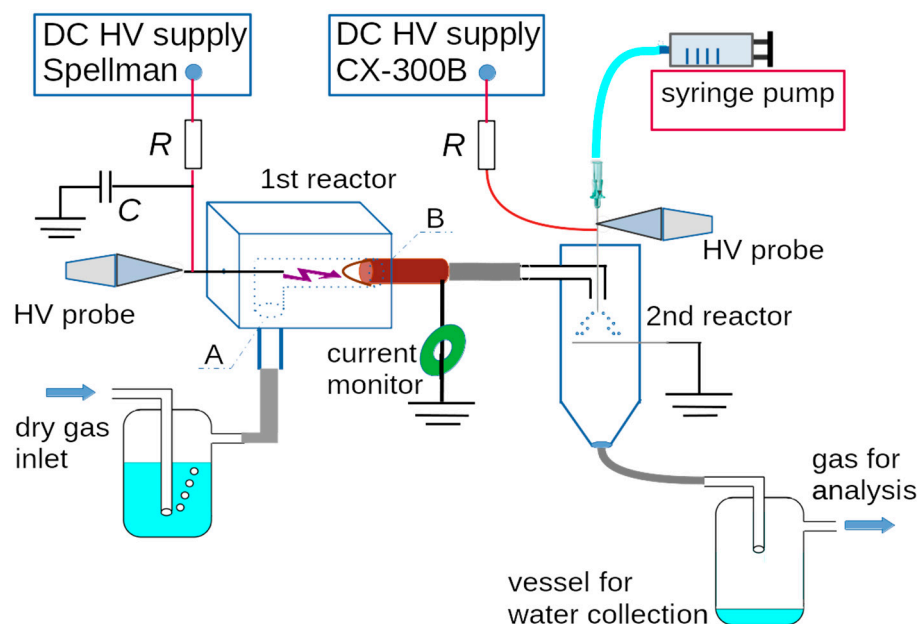


Figure 2. Simplified schematic of the experimental setup of two-stage system (2SS), with the first reactor for TS generation and the second reactor for water electrospray (ES); R—resistor, C—capacitor, HV—high voltage, A—opening for the gas inlet, B—opening for the gas outlet and insertion of the grounded electrode.

2.1. Reactor Details

The first reactor in 2SS (Figure 2) used for TS generation, has shape of a block with dimensions $16 \times 11 \times 43$ mm made of polytetrafluoroethylene (PTFE). Two intersecting perpendicular holes A and B (diameter 6 mm with M6 thread) are drilled in this block, so that the gas can pass through it, making 90 degree turn. One of these openings (B) serves for insertion of grounded electrode into the reactor. The grounded electrode is a copper wire with diameter 1 mm connected to the end of copper tube used for gas outlet, with the inner diameter 5 mm and outer diameter 6 mm and with outer M6 thread. There is another hole, with diameter 2 mm and M2 thread, opposite to the opening B. The M2 hole serves for insertion of stressed (anode) electrode, namely an iron M2 screw with a sharpened tip. The gap between the electrodes is approximately 10 mm.

The second reactor, used for ES in 2SS experiments (Figure 2) and for generation of both TS and ES in 1SS experiments (Figure 1), has a cylindrical shape with an inner diameter 2.9 cm and its length is 13 cm. The high voltage is applied to the top blunt hollow needle electrode (anode), having outer diameter 0.7 mm and inner diameter 0.5 mm. When this reactor is used as a second stage for generation of ES without TS (2SS experiments), a CX-300B DC HV power supply (unbranded, China) is used, connected to the anode via series resistor $R = 13.5$ M Ω . The applied voltage is 6 kV (below TS onset voltage) and it is monitored by a N2771A HV probe (Agilent, Santa Clara, CA, USA). The current was not measured in the second reactor when used only for ES generation without TS, because it was below the measurable limits of our current 2877 monitor (Pearson Electronics, Palo Alto, CA, USA).

The grounded electrode is also a medical needle with the outer diameter 0.7 mm going through the body of the reactor, with the gap between the electrodes being 10 mm. The top needle electrode (anode) is also used for the ES water input, continuously supplied with the deionized water (pH \sim 5.4, conductivity \sim 3 μ S/cm) by a NE-300 syringe pump (New Era Pump Systems, Farmingdale, NY, USA) through silicon tubing under controlled flow rate ($Q_w = 100$ –500 μ L/min). The treated gas enters the reactor in the upper part in direction parallel to the HV needle electrode, where it comes to contact with electrosprayed microdroplets. The water and the gas leave the reactor together at the bottom of the

cylindrical reactor. The water is collected in a vessel behind, while the gas continues towards the analytical part of the system. The openings in the reactor where needle electrodes are inserted are sealed by a vacuum grease to avoid leaks of a treated gas.

2.2. TS Generation and Diagnostics

A high voltage (HV) DC power supply (SL30P300 Spellman, Hauppauge, NY, USA) connected to the reactor via series resistor $R = 3.2 \text{ M}\Omega$ is used to generate positive polarity TS between two metallic electrodes in a pin-to-wire configuration. The distance between electrodes in both reactors is approximately 10 mm. The TS discharge characteristics were measured by a P6015A HV probe (Tektronix, Berkshire, UK) and a Pearson Electronics 2877 current monitor, and then processed by a TBS2104 digital oscilloscope (Tektronix).

Despite using DC power supply, TS is a self-pulsing discharge characterized by short high current pulses (Figure 3), with a typical repetition frequency $f = 1\text{--}10 \text{ kHz}$ [46,47]. Energy delivered to the plasma per pulse can be calculated from the measured current I and voltage V waveforms by the following formula:

$$E_p = \int_T V \times Idt \quad (2)$$

with the integration period T covering all the spark current pulse produced by discharging of the electric circuit capacity C . In our previous works we relied on internal capacity of the circuit, provided mostly by the HV cable connecting the anode with the ballast resistor R , with a length 1–2 m. Here we used a much shorter cable and thus we used an external capacitor $C = 50 \text{ pF}$ to provide a sufficient discharging capacity. Still, 50 pF is low enough to avoid classical spark discharge that generates a thermal plasma, because TS current pulses have too short duration and E_p is only around 2 mJ/pulse. Knowing E_p , the discharge power (p) can be obtained as a product of the repetition frequency times the energy delivered per pulse: $P = f \times E_p$. Finally, the input energy density E_d in [J/L] can be calculated as follows:

$$E_d = 60 \times P/q \quad (3)$$

where q is a gas flow rate in [L/min].

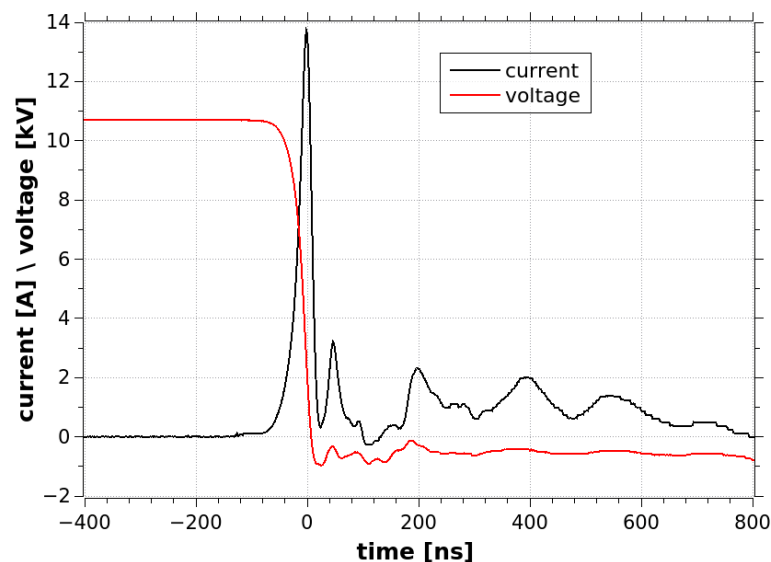


Figure 3. Typical current and voltage waveforms of the TS, short time scale showing the voltage drop and the current pulse associated with the gas breakdown.

2.3. Gas Phase Diagnostics

The analytical system for gas composition analysis consists of three stages. First, the gas leaving the plasma reactor entered a 10 cm long cell with inner diameter 2.5 mm,

used for UV-Vis absorption spectroscopy. As a light source, an AvaLight-D-S deuterium lamp (Avantes, Louisville, CO, USA) is used, along with an Avantes AvaSpec-Mini4096CL spectrometer for spectrally resolved light detection. Spectral resolution is 0.4–0.5 nm and spectra in the range 190–650 nm were recorded. Next, the analysed gas passes to the second, 75 cm long cell for UV-Vis absorption spectroscopy, with the same inner diameter 2.5 mm. As a light source, an Insight PX-2 pulsed Xe lamp (Ocean Insight, Orlando, FL, USA) is used here, with an Ocean Insight STS-UV spectrometer for spectrally resolved light detection. Spectral resolution is 3 nm and spectra in the range 185–665 nm are recorded. The UV-Vis absorption technique enables quantitative simultaneous detection of NO, NO₂, HNO₂ and O₃. Measurement in two absorption cells with different lengths serves to expand the dynamic range of the studied RONS from a few ppm up to more than 1000 ppm. For example, the 75 cm cell enables quantitative detection of NO approximately in the range 5–200 ppm, while the 10 cm cell expands the upper detection limit of NO up to ~1400 ppm.

The third technique used for analysis of treated gas was Fourier transform infrared (FT-IR) spectrophotometry (IRAffinity-1S with wavenumber range 7800–350 cm⁻¹ and a best spectral resolution of 0.5 cm⁻¹, Shimadzu, Kyoto, Japan). The absorption spectroscopy in IR region is more versatile, i.e., more compounds can be found in the spectra than in the UV-Vis region. Besides NO, NO₂, HNO₂ and O₃, detectable also in UV-Vis region, we can detect HNO₃, N₂O, CO, CO₂ and almost all volatile hydrocarbons. In practice, the variations of water vapor concentration during experiments with humid air and with ES makes analysis of FT-IR spectra more complicated. The obtained spectra are noisy, with more complicated baseline shifts. Moreover, the used spectrometer is very sensitive to the electromagnetic noise from TS.

Both FT-IR and UV-Vis absorption techniques are absolute. The concentration of studied RONS in the gas were obtained by fitting of measured spectra with synthetic spectra. In order to obtain synthetic FT-IR spectra, we downloaded set of absorption lines for NO, NO₂, H₂O, HNO₃, O₃ and H₂O₂ molecules from HITRAN database [48]. Next, we convoluted these absorption lines to match the calculated spectra with the spectra measured by our spectrometer for spectral resolution 1 cm⁻¹. We verified this approach by measurement of NO and NO₂ with known concentration from calibration pressure tanks. As there is no suitable set of absorption lines for HNO₂, we used absorption cross sections downloaded from supplemental HITRAN database [49].

The UV-Vis absorption cross sections of NO, NO₂, HNO₂, HNO₃, N₂O₄, O₃ and H₂O₂ were downloaded from the MPI-Mainz UV/VIS Spectral Atlas [50]. Next, we convoluted all absorption cross sections measured with better spectral resolution to fit spectral resolution of our spectrometers, keeping the area under the curve constant. Our approach was verified by using calibration pressure tanks with the known concentration of NO and NO₂.

Figure 4 shows an example of the experimentally obtained spectrum, fitted by synthetic spectra of NO₂, HNO₂, H₂O₂ and NO. We achieved very good agreement between experimental and synthetic spectra by combined absorption of NO₂, HNO₂, NO and H₂O₂ molecules. The H₂O₂ absorption cross sections helped us to fit the spectrum in the range 200–280 nm, although the obtained concentrations of H₂O₂ are not presented in this paper because the H₂O₂ absorption cross section has no specific pattern and N₂O, N₂O₄, or HNO₃ have very similar cross sections. Absorbance in this part of the spectrum is also influenced by humidity inside the absorption cell.

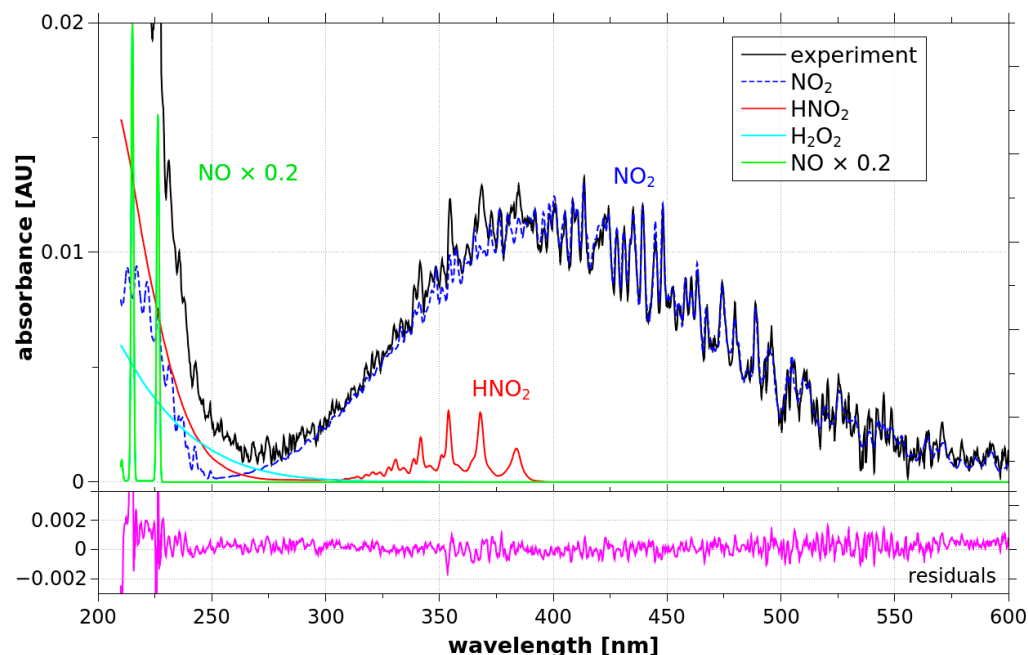


Figure 4. Typical UV-Vis absorption spectrum measured in 10 cm long cell, humid air treated by TS, mean current 2 mA, compared with synthetic spectra of NO_2 , HNO_2 , H_2O_2 and NO . Bottom chart shows residuals in experimental spectrum after subtraction of all synthetic spectra.

2.4. Analysis of Water

The pH of collected plasma-activated water (PAW) was measured by a calibrated pH-EC-TDS-TEMP pH multimeter (EZ-9908, unbranded, China), and the concentrations of NO_2^- (aq) and $\text{H}_2\text{O}_{2(\text{aq})}$ formed in water were detected by the colorimetric methods using the Shimadzu UV-1800 UV/VIS absorption spectrophotometer. A Nitrate/Nitrite Colorimetric Assay Kit (# 780001, Cayman Chemicals, Ann Arbor, MI, USA) with ready-to-use Griess reagents was used for a quantitative analysis of NO_2^- (aq). The Griess assay method is the most commonly used for NO_2^- (aq) detection in plasma-activated solutions [51–57]. In the Griess diazotization reaction, NO_2^- (aq) reacts with sulfanilic acid under acidic conditions to form a diazonium ion, which couples to α -naphthylamine to form a readily water-soluble, deep purple colored azo dye, with the absorption maximum at 540 nm. The specificity and accuracy of the Griess assay for the detection of NO_2^- (aq) in PAW was confirmed by ion chromatography [58].

Measurement of $\text{H}_2\text{O}_{2(\text{aq})}$ was performed by the titanium oxysulfate assay based on the reaction of $\text{H}_2\text{O}_{2(\text{aq})}$ with the titanium (IV) ions under acidic conditions. The yellow-colored product of pertitanic acid H_2TiO_4 is formed with the absorption maximum at 407 nm [59]. The concentration of $\text{H}_2\text{O}_{2(\text{aq})}$ is proportional to the absorbance according to Lambert–Beer’s law (molar extinction coefficient $\epsilon = 6.89 \times 10^2 \text{ L mol}^{-1} \text{ cm}^{-1}$). Because of the possible $\text{H}_2\text{O}_{2(\text{aq})}$ decomposition by NO_2^- (aq) under acidic conditions, sodium azide (NaN_3 , 60 mM) was added to the sample prior to mixing with the titanium oxysulfate reagent [19]. Sodium azide immediately reduces NO_2^- (aq) into molecular nitrogen and preserves the $\text{H}_2\text{O}_{2(\text{aq})}$ concentration intact.

3. Results and Discussion

TS generates a highly reactive non-equilibrium plasma (despite a very short temporary gas temperature increase during the spark phase [47]), with chemical effects comparable to plasmas generated by short HV pulses [60]. One of the advantages of the TS in comparison with discharges generated by short HV pulses is its capability of simultaneous generation of the plasma and the ES of water through the discharge zone. ES cannot be induced by short voltage pulses applied to the needle. In the TS, the voltage on the hollow needle

electrode is not constant, but it is high enough to induce formation of microdroplets most of the time, except during the short period after voltage drops associated with gas breakdown (Figure 5a).

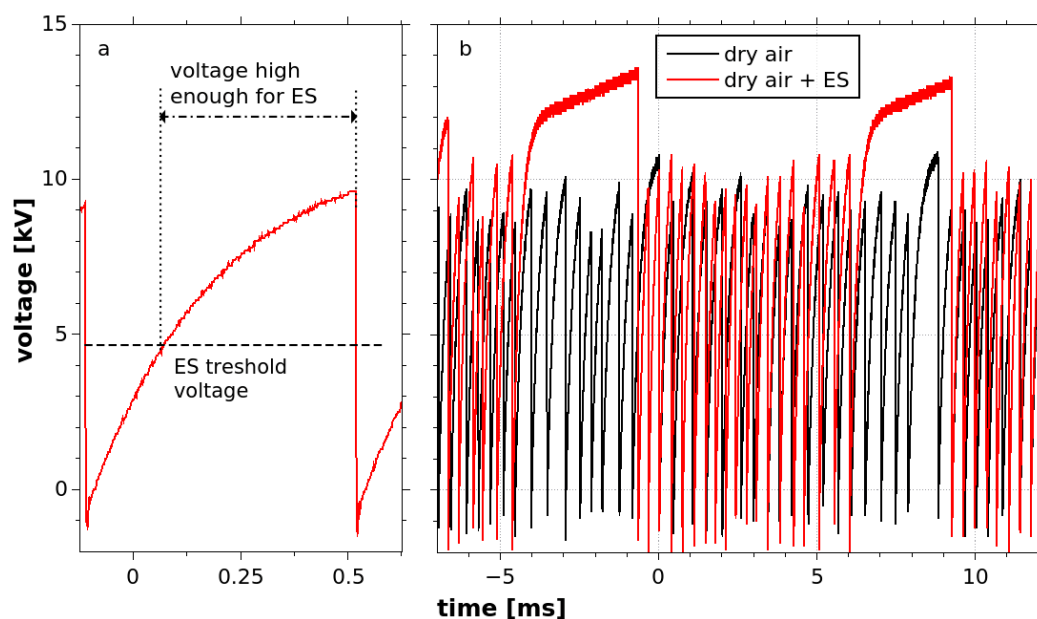


Figure 5. Typical long timescale TS voltage waveforms; (a) voltage increase regrowth between two voltage drops (gas breakdowns, i.e., TS pulses), showing that voltage is high enough for formation of microdroplets by ES most of the time; (b) voltage waveforms showing several tens of breakdowns, comparison of voltage waveforms without (black) and with ES (red; water flow rate $Q_w = 300 \mu\text{L}/\text{min}$) where periods without breakdowns and TS current pulses appear (e.g., time period 6–9 ms).

However, we must consider that TS and ES influence each other. This mutual influence causes instabilities of both ES and TS. Stable steady-state ES can be achieved only without a discharge or with a pulseless discharge, such as glow corona [61]. Vice-versa, the water flow needed for the ES causes instabilities of the TS, as shown in Figure 5b with periods where voltage increases well above the TS onset voltage (~ 10 kV), but no voltage drops associated with TS current pulses (e.g., time period 6–9 ms on Figure 5b). During these periods, only corona discharge may be generated, with much lower power and almost no generation of nitrogen oxides. Moreover, due to these corona discharge periods, the uncertainty of f in TS combined with ES is higher than in TS without ES. As a result, the uncertainty of the input energy density E_d is higher, causing a worse repeatability of experimental results. Nevertheless, it is still possible to compare generation of RONS by TS with and without ES, as shown in the Section 3.1.

The formation of RONS in the gas phase as described in Section 3.1 is just the first step in PAW generation. The second step is the solvation of gaseous RONS into water microdroplets. The changes of gaseous RONS concentrations caused by ES of water are described in Section 3.2. Finally, the Section 3.3 shows results from the analysis of generated PAW, explaining importance and contribution of individual RONS generated by TS (NO , NO_2 and HNO_2) on the achieved concentration of NO_2^- (aq).

3.1. Generation of RONS in the Gas Phase

The analytical method we used enables the detection of various RONS. In the dry air treated by the TS we detected only three long-lived species: NO , NO_2 and traces of HNO_2 . Other possible RONS, such as O_3 or HNO_3 were not detected. NO is a dominant product of the air TS plasma with the highest concentration achieved. The concentration of NO

grows almost linearly with increasing input energy density, and the concentration of NO using either dry or humid air are almost identical (Figure 6).

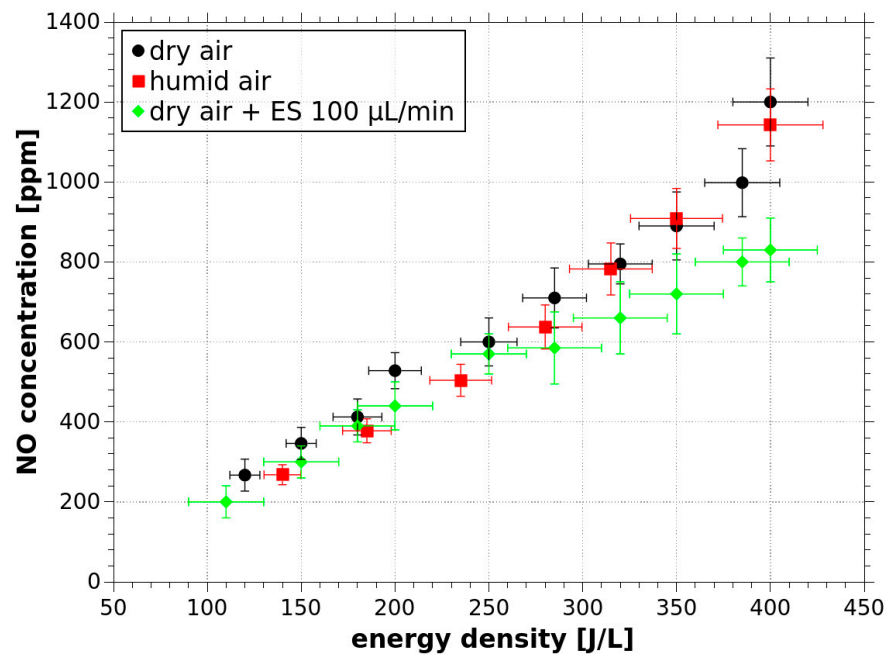


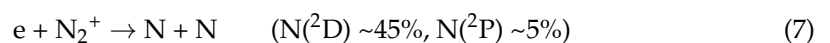
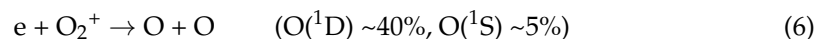
Figure 6. NO concentration as a function of the TS input energy density, measured by UV-Vis absorption technique, short absorption cell, ISS.

Based on preliminary results from chemical kinetic model of TS [62], we assume that NO is generated by the modified Zeldovich mechanism. The original Zeldovich mechanism is initiated by the thermal decomposition of N_2 and O_2 into their atomic states at high temperature (above ~ 1500 K). Despite the fact that TS generates ‘cold’ non-equilibrium plasma, the temperature during the short spark phase of the TS can be as high as ~ 3000 K [47]. Next, both N and O atomic radicals are able to produce NO:



The rate coefficient of Reaction (5) with N atoms is four orders of magnitude higher at 3000 K than at room temperature, but the production of N atomic radicals via the thermal decomposition of N_2 is very slow, even at 3000 K (rate coefficient $\sim 1.5 \times 10^{-24} \text{ cm}^3 \text{ s}^{-1}$) [63]. As a result, the thermal decomposition of N_2 is a rate-limiting step of the thermal NO formation. In the TS discharge, the thermal mechanism of NO formation is bypassed by alternative reaction pathways for the generation of N and O atomic radicals. The influence of spark on plasma induced chemistry is not based on gas heating only, more important is an achievement of a high degree of ionization, with the electron density $n_e > 10^{17} \text{ cm}^{-3}$ [64].

The high degree of ionization results in a high degree of atomization thanks to the dissociative electron-ion recombination reactions:



In the next step, the products of reactions (6) and (7) enhance the NO synthesis, especially by N production bypassing the rate limiting step in the Zeldovich mechanism by Reaction (4). Moreover, reactions (4) and (5) can be much faster if one of the reactants is in an excited state [63,65]. There are many other reactions that can contribute to N or O

atoms production. For example, additional O atoms can also be created from O₂ molecules by dissociative electron attachment reaction.

A few microseconds after the spark current pulse, air cools down and the N concentration decreases. Consequently, the NO production stops. Remaining O atoms start to generate ozone O₃:



Alternatively, the atomic oxygen can oxidize NO to form NO₂ in a three-body Reaction (9):



However, Reaction (8) producing O₃ is faster. Consequently, O₃ also oxidizes NO to NO₂:



As a result, NO₂ is a product with the second highest measured concentration (Figure 7). In dry air, there are no other significant products of TS.

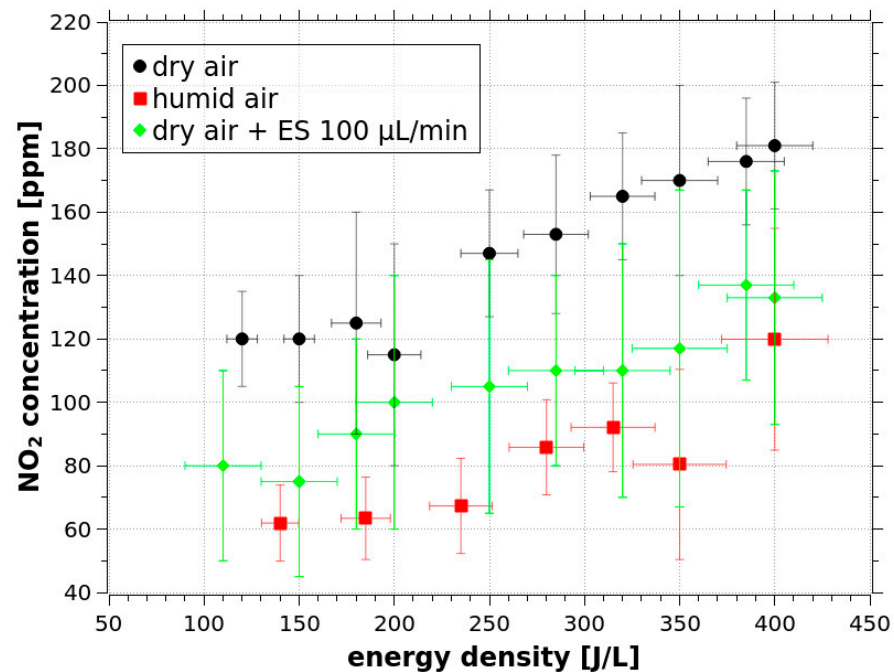


Figure 7. NO₂ concentration as function of the TS input energy density, measured by UV-Vis absorption technique, short absorption cell, 1SS.

We observed no O₃ at the outlet, probably because Reaction (10) is fast enough and there is a sufficient amount of NO so that O₃ is fully consumed by the oxidation of NO to NO₂ before the gas enters the closest UV absorption cell (the estimated delay between the moment when air is treated by the discharge and when it is analyzed in the short UV cell is 17–20 s). If we assume that Reaction (10) is a dominant source of NO₂, the achieved NO₂ concentration (~100–200 ppm, Figure 7) should be approximately equal to concentration of formed and immediately consumed O₃. To understand O₃ formation without its depletion by NO, we performed experiments in 1SS with TS operating in dry O₂. These experiments proved that TS can really generate high concentration of O₃ (Figure 8), when it is not consumed by reaction with NO.

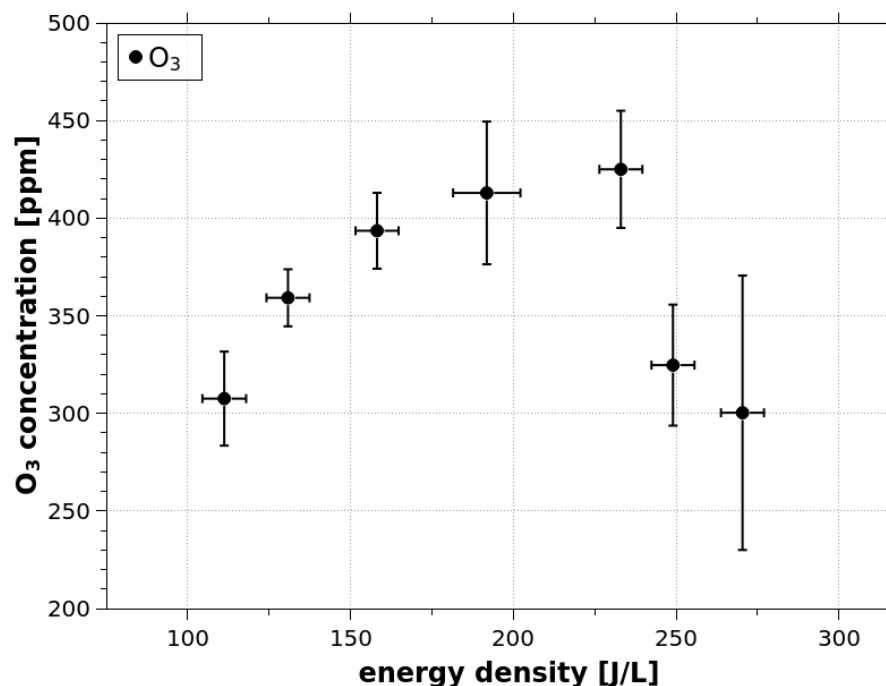


Figure 8. O₃ concentration as a function of the TS input energy density, dry O₂ treated by TS in 1SS without ES, measured by UV-Vis absorption technique, short absorption cell.

We also performed experiments in humid O₂, where the electron impact reaction with H₂O can result into several radicals (OH, H) or ions (O⁻, OH⁻, H₂O⁺) [66,67]. The OH radicals can be also created by collisions of H₂O with O(¹D) species. Next, H and OH radicals can decompose O₃ in the reactions:



For this reason, the concentration of O₃ generated in humid O₂ was approximately 15 times lower than in dry O₂. We can also expect lower production of O₃ in the humid air compared to dry air. In turn, lower production of O₃ could explain why the presence of humidity in air decreased the NO₂ concentration (Figure 7). However, the concentration of NO₂ in humid air was not 15 times lower than in dry air. It is probably because NO₂ may be also generated by different reaction channels, for example by the reaction with HO₂ radical. Sufficient amount of HO₂ radicals may be provided by reaction of OH radicals with O₃ (Equation (12)), or with H₂O₂.

The presence of OH radicals influences the reaction mechanism even more significantly by the reaction:



leading to the formation of HNO₂. In the humid air treated by TS, the HNO₂ concentration becomes comparable to NO₂ concentration (Figure 9). Some HNO₂ was observed in dry air as well, showing a significant influence of even minor H₂O impurities (from the carrier gas and/or due to desorption from surfaces) on NO, NO₂ and HNO₂ generation chemistry.

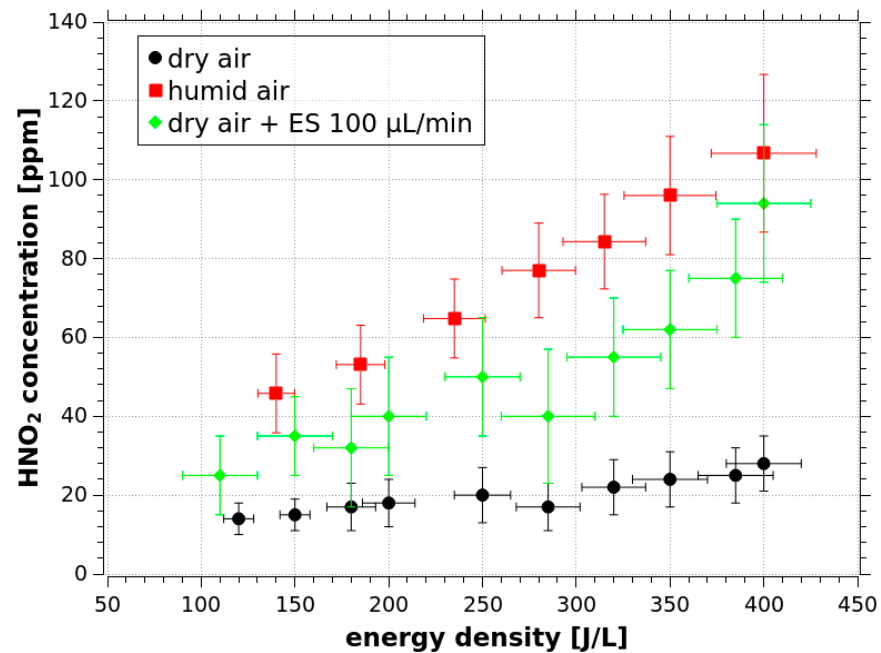


Figure 9. HNO_2 concentration as function of the TS input energy density, measured by UV-Vis absorption technique, short cell, 1SS.

Overall, the sum of NO_2 and HNO_2 concentrations (H_yNO_2) is almost equal in humid and dry air, only below $E_d \sim 250$ J/L it is slightly lower in humid air compared to dry air. The total amount of H_yNO_x ($\text{NO} + \text{NO}_2 + \text{HNO}_2$) is within the experimental uncertainty the same in the entire range of E_d (Figure 10).

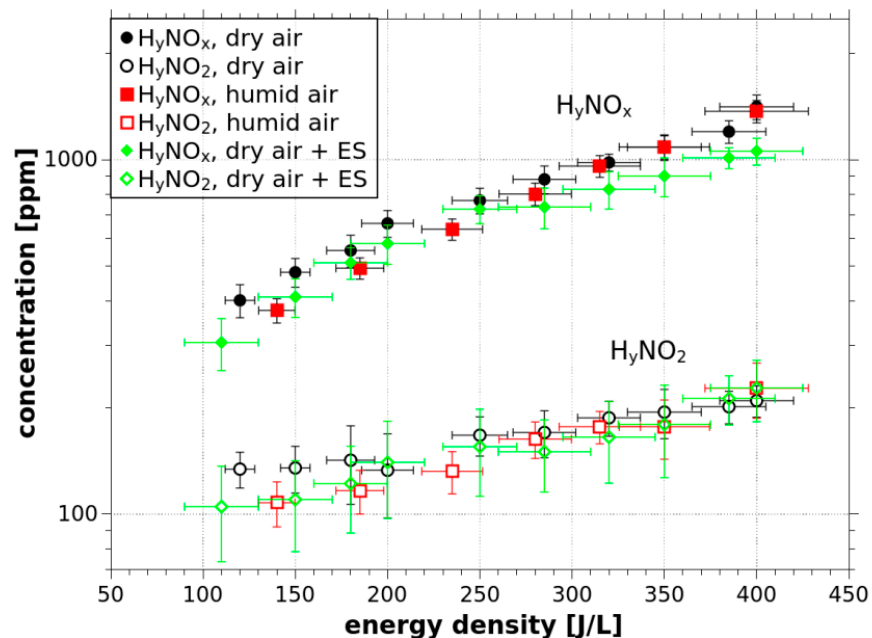
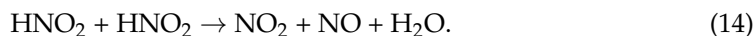


Figure 10. H_yNO_2 ($\text{HNO}_2 + \text{NO}_2$) and H_yNO_x ($\text{HNO}_2 + \text{NO}_2 + \text{NO}$) concentrations as functions of the TS input energy density, comparison of dry air, humid air, and dry air + ES, measured by UV-Vis absorption technique, short cell, 1SS.

The total amount of H_yNO_x is constant in time as well, based on comparison of concentrations obtained in short UV-Vis absorption cell and concentrations measured by FT-IR spectrometry. However, the ratio of individual components slightly changes. The

NO₂ concentration increases, while the concentrations of NO and HNO₂ slightly decrease. The decomposition of HNO₂ may proceed via the following reaction:



Taking into account the instability of HNO₂ molecules, we can deduce that their concentration is higher inside the reactor than when measured in the short UV absorption cell. Nonetheless, the measured concentration of HNO₂ is so high that HNO₂ probably plays a major role in PAW generation by TS with ES, because it has a much higher solubility than NO₂ and NO. Thus, the concentration of RONS in TS with ES is not influenced only by chemical reactions (11)–(14), but also by the solvation processes discussed in Section 3.2.

3.2. Solvation of Gaseous RONS to ES Microdroplets

The solubility of gases depends on their Henry's law coefficient. NO, NO₂ and HNO₂ generated by TS differ significantly from the solubility point of view. The solubility of NO is the lowest (with Henry's law coefficient $k_H = 0.0018 \text{ mol kg}^{-1} \text{ atm}^{-1}$ at 298.15 K [44]). It is easy to show that in an experiment with gas flow 1.1 L/min and water flow rate 100 $\mu\text{L}/\text{min}$, even if we achieve a saturated NO solution, the decrease of the gas phase concentration of NO is not detectable as it is much smaller than the accuracy of our analytic techniques. Thus, the decrease of NO concentration generated by TS in dry air with ES compared to the results without ES (Figure 6), cannot be explained by the solvation of NO into water.

We assume that there are other processes responsible for this NO decrease. We must consider instabilities of TS caused by the water flow supplied for the ES, as shown in Figure 5b with long time scale voltage waveforms. Taking into account the appearance of short periods without spark pulses and energy consumed on evaporation of the sprayed microdroplets, we assume that water sprayed into the discharge has a cooling effect. This could explain a lower efficiency of TS to generate NO at higher input energy densities (Figure 6).

The solubility of NO₂ is slightly higher than the solubility of NO, almost by about one order of magnitude. However, the decrease of NO₂ in the experiment with ES compared to the dry air (Figure 7) also cannot be dominantly due to the NO₂ solvation to liquid water. Moreover, there was even less NO₂ in the experiment in humid air than in dry air or air with ES. We thus suppose that the observed changes of NO₂ concentration are rather related to the shift in NO₂/HNO₂ formation chemistry due to the presence of H₂O (reactions (11)–(14)).

The solubility of HNO₂ is much higher (by three orders of magnitude) than the solubility of NO₂. Thus, it is possible that the measured gaseous HNO₂ concentration is influenced by the solvation effect. However, it is questionable since the sum of NO₂ and HNO₂ (H_yNO₂) is the same in all experiments (Figure 10). It is therefore possible that the decrease of HNO₂ in the experiment in dry air with ES compared to the experiment in humid air is caused by the change in NO₂/HNO₂ chemistry due to differences in the humidity.

In the single reactor experiments in 1SS, when comparing the results with and without ES, it is impossible to separate changes of NO₂ and HNO₂ concentrations due to solvation to water, changes in chemical pathways of their formation and decay, cooling effect of water, or discharge instabilities. In order to assess the role of individual RONS in PAW generation, additional experiments were performed in 2SS with two reactors. The synthetic air (dry or humidified) was treated by TS in the first reactor. This treated air containing HyNO_x was lead as the inlet gas into the second reactor with ES but without TS. We measured changes of the gas composition and aqueous NO₂[−](aq) and H₂O₂(aq) in the accumulated water (see Section 3.3).

Figure 11 shows the comparison of NO concentration generated by TS in dry and humid air in 2SS with and without ES treatment in the second reactor (water flow rate 500 $\mu\text{L}/\text{min}$).

These results confirm a low solubility of NO, because its concentration in gas is within the experimental uncertainty not influenced by ES, both for dry and humid air.

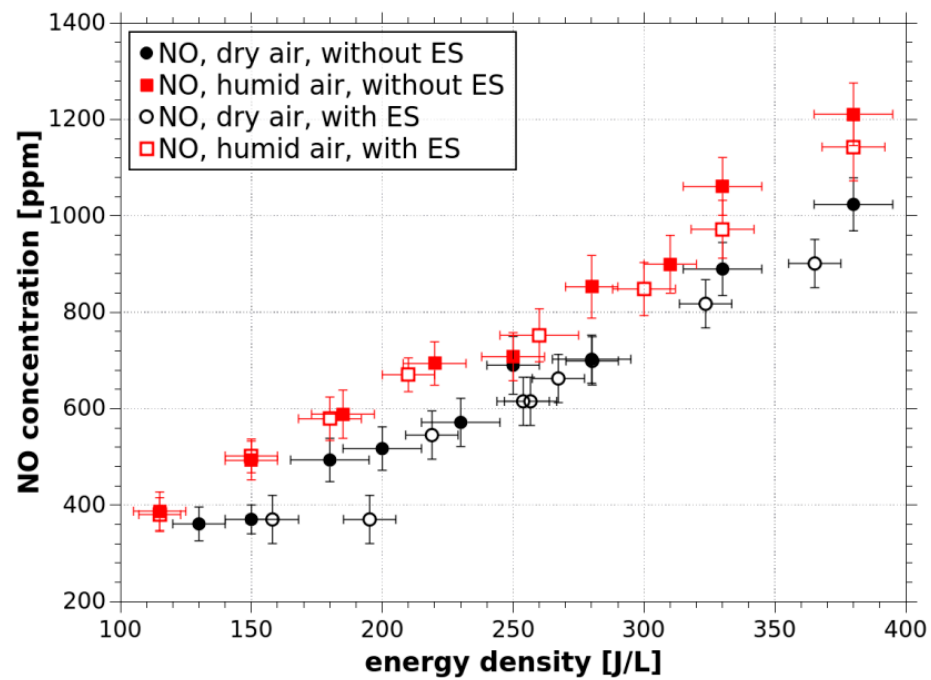


Figure 11. Comparison of NO concentration produced by TS in the first reactor, with and without ES ($Q_w = 500 \mu\text{L}/\text{min}$) in the second reactor (2SS), measured by UV-Vis absorption technique, short cell.

The solubility of NO_2 is almost by one order of magnitude higher than the solubility of NO. There is probably some decrease of NO_2 due to post-discharge ES treatment, especially at higher energy densities, i.e., when the NO_2 concentration is higher (Figure 12).

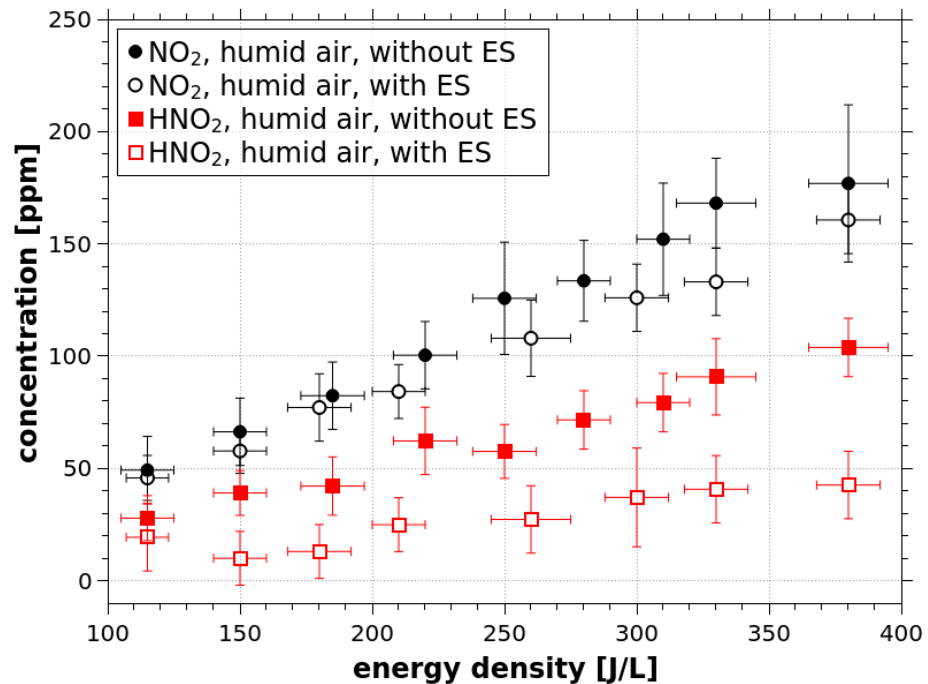


Figure 12. Comparison of NO_2 and HNO_2 concentration with and without post discharge ES treatment, measured by UV-Vis absorption technique, short cell, 2SS.

However, the decrease is still not significant with respect to the experimental uncertainty. The decrease of HNO_2 due to ES is more remarkable, despite that after the ES treatment in the second reactor, the HNO_2 concentration is already quite low and the relative experimental uncertainty is higher. These results indicate the key importance of HNO_2 for PAW generation, which is further confirmed by the PAW analysis.

3.3. Analysis of Plasma-Activated Water

We measured $\text{NO}_2^-_{(\text{aq})}$ and $\text{H}_2\text{O}_{2(\text{aq})}$ in plasma-activated water collected during 1SS experiments with TS combined with ES, as well as in water collected during 2SS experiments, with TS and ES separated into two reactors. As for control, we also performed experiments in 1SS with ES, but without TS. The used gas was either synthetic air (dry or humidified), or NO and NO_2 from calibration pressure tanks, mixed with N_2 or synthetic air, respectively.

In the control experiments with ES, the applied voltage (6 kV) was not sufficient for TS generation, but it was above the onset voltage of the corona discharge. Due to this, there was probably some formation of reactive species inside the ES reactor, and we detected a low concentration of $\text{H}_2\text{O}_{2(\text{aq})}$, $\sim 20 \mu\text{M}$. This weak corona discharge in air, however, produced no detectable amount of nitrogen oxides and no $\text{NO}_2^-_{(\text{aq})}$ was detected in water.

Relatively small amount of $\text{NO}_2^-_{(\text{aq})}$ ($\sim 80 \mu\text{M}$, Figure 13, red point) was detected in control experiment in 1SS with ES and without TS, using gas from the pressure tank containing ~ 1400 ppm NO in N_2 . This proves a low solubility of NO. The formation of $\text{NO}_2^-_{(\text{aq})}$ from the dissolved $\text{NO}_{(\text{aq})}$ proceeds via the following reaction:

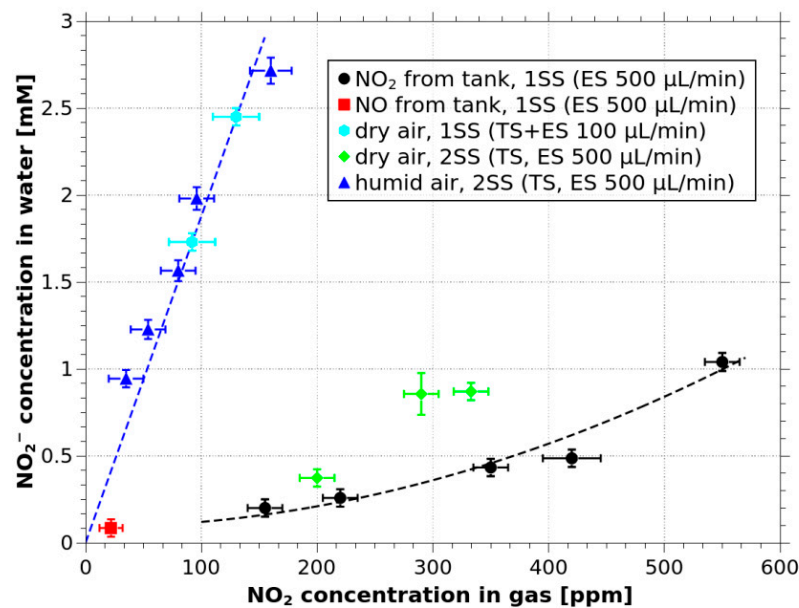
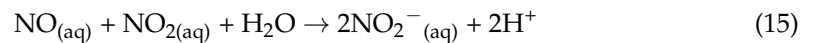
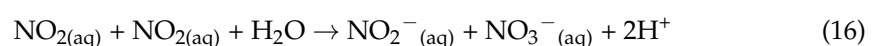


Figure 13. Concentration of $\text{NO}_2^-_{(\text{aq})}$ in collected water as function of gas phase NO_2 concentration, ES with $Q_w = 500 \text{ uL/min}$, different gas mixtures, and combined TS with ES ($Q_w = 100 \text{ uL/min}$).

Thus, the dissolved $\text{NO}_{2(\text{aq})}$ is also needed to produce $\text{NO}_2^-_{(\text{aq})}$. In the gas phase only around 25 ppm NO_2 was detected and this limited the $\text{NO}_2^-_{(\text{aq})}$ production. We can conclude that without NO_2 , even very high concentration of NO has almost a negligible effect on the aqueous RONS formation. On the other hand, the solvation of NO_2 from the gas phase into water can lead to $\text{NO}_2^-_{(\text{aq})}$ formation even without a presence of $\text{NO}_{(\text{aq})}$, via the following reaction:

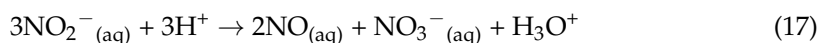


One NO_2^- (aq) molecule is produced from two dissolved NO_2^- (aq) molecules. If we assume that NO_2^- (aq) is proportional to the gas phase NO_2 concentration, Reaction (16) could explain why the measured concentration of NO_2^- (aq) in water can be well fitted as a quadratic function of the gas phase NO_2 concentration (Figure 13, black points), when NO_2 from the pressure tank mixed with dry synthetic air was used.

In the dry synthetic air treated by TS in the first reactor and ES in the second reactor (2SS), the measured concentration of NO_2^- (aq) in water was higher, above the fitting curve valid for NO_2 from the pressure tank (Figure 13, green points). We assume that it can be explained by the presence of both NO and NO_2 in the sprayed gas, i.e., both NO and NO_2 can also contribute to the NO_2^- (aq) formation via Reactions (15) and (16).

If NO_2 in the gas phase plays a dominant role on NO_2^- (aq) formation in water, one could expect less NO_2^- (aq) in the water collected during 2SS experiments in humid synthetic air, where the gas phase NO_2 concentration produced by TS in the first reactor was lower compared to that generated by TS in the dry air. On the contrary, significantly higher NO_2^- (aq) concentration was observed (Figure 13, blue points). Here, the TS discharge in the first reactor generated not only NO and NO_2 , but also directly by gaseous HNO_2 , which can then form NO_2^- (aq) directly by its rapid solvation into water microdroplets generated by ES in the second reactor. Figure 13 shows an approximately linear dependence of NO_2^- (aq) on gaseous NO_2 when applying ES in humid air treated by TS. This most likely indicates a linear dependence of NO_2^- (aq) on the gaseous HNO_2 concentration, since HNO_2 concentration is proportional to the NO_2 concentration (Figure 12).

If we assume that the amount of NO_2^- (aq) in the liquid phase is proportional to the depletion of HNO_2 from the gas phase, we can estimate the expected NO_2^- (aq) concentration in the water. The highest HNO_2 decrease observed was approximately 50 ± 10 ppm. Taking into account gas and water flow rates, the corresponding estimated NO_2^- (aq) concentration in the liquid phase should be 4.4 ± 0.9 mM. The measured NO_2^- (aq) concentration was somewhat lower: 2.7 ± 0.2 mM. This difference could be explained by the instability of NO_2^- (aq) at acidic conditions, because the measured pH = 2.5–2.8 in the collected water. The disproportionation reaction:



leads to exponential-like NO_2^- decrease in time. In PAW generated by TS, the observed characteristic decay time was approximately 30–40 min [58]. In our experiments in 2SS, the collected water sample was mixed with Griess reagent within 5 min after the end of the experiment. During this time, the NO_2^- concentration could decrease approximately by about 20% from the concentration reached at the moment when the experiment was stopped. Moreover, conversion of NO_2^- (aq) to NO_3^- (aq) also occurs during the time of experiment (4 min) inside the vessel where the water accumulates. Taking into account the NO_2^- (aq) concentration decrease due to Reaction (17) and the experimental uncertainty, the agreement between the measured NO_2^- (aq) concentration and the estimated one from the HNO_2 depletion from the air is satisfactory.

In the previous paragraphs we have discussed and compared differences of NO, NO_2 and HNO_2 solubility, and we based our reasoning mainly on differences of Henry's law coefficients of these three species. As mentioned in the Introduction, the Henry's law coefficient is valid for systems in a thermodynamic equilibrium and in plasma-water interactions, the solvation process may be influenced by many other phenomena. Here we must emphasize that in 2SS, the plasma and water did not interact directly. Direct interaction of plasma with water microdroplets occurred only in 1SS. However, the concentration of NO_2^- (aq) in PAW generated in 1SS with a direct contact of TS with microdroplets is not higher than NO_2^- (aq) concentration achieved in 2SS experiments in humid air with TS and ES separated into two reactors. It shows the same trend and similar values (Figure 13, cyan vs. blue points). This result justifies the reasons to compare solubility of species with long lifetime based on their Henry's law coefficient.

The major difference between PAW generated by TS with simultaneous ES (1SS), and water prepared in 2SS by spraying humid air treated by TS in the first reactor, is the concentration of produced $\text{H}_2\text{O}_{2(\text{aq})}$. In the latter case the $\text{H}_2\text{O}_{2(\text{aq})}$ concentration was only around 20 μM , while the concentration of $\text{H}_2\text{O}_{2(\text{aq})}$ in PAW generated by TS with ES was higher, 60–80 μM . This result can be interpreted so that $\text{H}_2\text{O}_{2(\text{aq})}$ is created mainly by solvation of OH radicals with short lifetime and therefore their concentration in the second reactor of 2SS is negligible. However, we must admit that this is just an assumption that must be verified by additional measurements.

Another interesting fact concerning $\text{H}_2\text{O}_{2(\text{aq})}$ is its very low concentration compared to $\text{NO}_2^-_{(\text{aq})}$. In our previous research we showed that TS in an open-air reactor can generate PAW with significantly higher $\text{H}_2\text{O}_{2(\text{aq})}$ concentration, exceeding the concentration of $\text{NO}_2^-_{(\text{aq})}$ [15]. The $\text{NO}_2^-_{(\text{aq})}/\text{H}_2\text{O}_{2(\text{aq})}$ ratio was approximately 3:7. In a closed reactor, with higher concentration of NOx in the gas phase, this ratio was much different, approximately 15:1 in favor of $\text{NO}_2^-_{(\text{aq})}$. Here, with even higher concentrations of NOx in the gas phase, the $\text{NO}_2^-_{(\text{aq})}/\text{H}_2\text{O}_{2(\text{aq})}$ ratio is even higher, approximately 30–40:1. We therefore suppose that new results presented in this paper are consistent with the previous observations. However, we must admit that the low concentration of $\text{H}_2\text{O}_{2(\text{aq})}$ in PAW with very high concentration of $\text{NO}_2^-_{(\text{aq})}$ and acidic pH can be also explained by a partial depletion of $\text{H}_2\text{O}_{2(\text{aq})}$ by its reaction with $\text{NO}_2^-_{(\text{aq})}$ during the liquid sample accumulation and processing.

4. Conclusions

Transient spark (TS) discharge in air turns out to be a very efficient source for generation of nitrogen oxides NO and NO_2 . More than 1000 ppm of NO was generated with an input energy density of 400 J/L. It was shown that in humid air, the TS discharge also generates a significant amount of HNO_2 , providing 10–100 ppm of HNO_2 depending on the input energy density.

The air TS discharge in contact with water is very suitable for the generation of plasma-activated water (PAW), because TS can operate in a direct contact with water electrosprayed (ES) into the discharge zone. The formation of microdroplets with high interface surface area facilitates the transfer of reactive species from plasma into water. HNO_2 was also detected in air treated by TS in combination with water ES in one-stage system (1SS). This indicates an important role of HNO_2 in PAW generation, because HNO_2 , although directly produced at lower concentrations, is much more soluble than two other major gas phase species generated by TS, NO and NO_2 .

To assess the role of HNO_2 , measurements were performed in two-stage system (2SS), where dry or humid air was treated by TS in the first reactor and water ES was applied in the second reactor. The dry air treated by TS in the first reactor contained mainly NO and NO_2 with only traces of HNO_2 , while in the humid air, NO_2 decreased and HNO_2 reached almost the same concentration of as that of NO_2 . For comparison, we also applied ES on NO and NO_2 from pressure tanks diluted in N_2 or air, respectively. These experiments confirmed that solvation to ES microdroplets caused a significant depletion of HNO_2 from the gas phase, while the depletion of NO was not observed, and the decrease of the NO_2 concentration was questionable.

The importance of HNO_2 for PAW generation by TS in air was proved by the measured concentrations of $\text{NO}_2^-_{(\text{aq})}$ in water. The concentration of $\text{NO}_2^-_{(\text{aq})}$ was much higher in humid air containing HNO_2 than in dry air with higher concentration of NO_2 , but almost no HNO_2 in 2SS experiments with TS in the first reactor and ES in the second reactor.

The $\text{NO}_2^-_{(\text{aq})}$ concentration in 2SS experiments in humid air was similar (or even higher) than $\text{NO}_2^-_{(\text{aq})}$ concentration in PAW generated by a direct contact of the plasma with microdroplets in 1SS. The advantage of using 2SS is the stability and repeatability of the process. The TS in humid air without ES microdroplets inside the first reactor is relatively stable and the stable ES of water with higher water flow rate can be also achieved without TS in the second reactor. On the contrary, in 1SS with a direct contact of the

discharge with water, the ES and TS negatively influence each other and both ES and TS are less stable. However, the advantage of using 1SS with generation of TS and ES in the same reactor is reaching a higher concentration of H₂O₂ in the water.

The optimization of the HNO₂ generation by TS and of the 2SS with a shorter distance between TS and ES reactors are planned in future. Further research of undergoing chemistry is also desirable, both experimentally and by chemical kinetic modeling. Comparison of biocidal effects of PAW generated in 1SS and 2SS should be also performed to investigate the role of low vs. high H₂O_{2(aq)} concentration in addition to NO_{2⁻(aq)}. Nevertheless, this experimental study showed that gaseous HNO₂ produced in plasma discharges operated in humid air is a dominant contributor of nitrites in the plasma-activated water.

Author Contributions: Conceptualization, M.J., Z.M. and K.H.; methodology, M.J., K.H., P.T. and Z.M.; software, M.J.; validation, M.J. and P.T.; formal analysis, M.J. and P.T.; investigation, M.J., M.E.H. and P.T.; resources, M.J., K.H. and Z.M.; data curation, M.J., M.E.H. and P.T.; writing—original draft preparation, M.J.; writing—review and editing, Z.M., K.H., M.J. and M.E.H.; visualization, M.J.; supervision, Z.M., K.H. and M.J.; project administration, K.H. and M.J.; funding acquisition, Z.M. and M.J. All authors have read and agreed to the published version of the manuscript.

Funding: This research was funded by Slovak Research and Development Agency, grant number APVV-17-0382, and Slovak Grant Agency VEGA, grant number 1/0419/18.

Institutional Review Board Statement: Not applicable.

Informed Consent Statement: Not applicable.

Data Availability Statement: The data that supports the findings of this study are available within the article. Additional data that support the findings of this study are available from the corresponding author upon reasonable request.

Conflicts of Interest: The authors declare no conflict of interest.

References

1. Brandenburg, R.; Bogaerts, A.; Bongers, W.; Fridman, A.; Fridman, G.; Locke, B.R.; Miller, V.; Reuter, S.; Schiorlin, M.; Verreycken, T.; et al. White paper on the future of plasma science in environment, for gas conversion and agriculture. *Plasma Process. Polym.* **2019**, *16*, 1700250. [\[CrossRef\]](#)
2. Cvelbar, U.; Walsh, J.L.; Cernak, M.; De Vries, H.W.; Reuter, S.; Belmonte, T.; Corbella, C.; Miron, C.; Hojnik, N.; Jurov, A.; et al. White paper on the future of plasma science and technology in plastics and textiles. *Plasma Process. Polym.* **2019**, *16*, 1700228. [\[CrossRef\]](#)
3. Bekeschus, S.; Favia, P.; Robert, E.; Von Woedtke, T. White paper on plasma for medicine and hygiene: Future in plasma health sciences. *Plasma Process. Polym.* **2019**, *16*, 1800033. [\[CrossRef\]](#)
4. Von Woedtke, T.; Reuter, S.; Masur, K.; Weltmann, K.-D. Plasmas for Medicine. *Phys. Rep.* **2013**, *530*, 291–320. [\[CrossRef\]](#)
5. Keidar, M. Plasma for cancer treatment. *Plasma Sources Sci. Technol.* **2015**, *24*, 033001. [\[CrossRef\]](#)
6. Lu, X.; Ye, T.; Cao, Y.; Sun, Z.; Xiong, Q.; Tang, Z.; Xiong, Z.; Hu, J.; Jiang, Z.; Pan, Y. The roles of the various plasma agents in the inactivation of bacteria. *J. Appl. Phys.* **2008**, *104*, 053309. [\[CrossRef\]](#)
7. Lukes, P.; Clupek, M.; Babicky, V.; Sunka, P. Ultraviolet Radiation from the Pulsed Corona Discharge in Water. *Plasma Sources Sci. Technol.* **2008**, *17*, 024012. [\[CrossRef\]](#)
8. Dobrynin, D.; Fridman, G.; Friedman, G.; Fridman, A. Physical and Biological Mechanisms of Direct Plasma Interaction with Living Tissue. *New J. Phys.* **2009**, *11*, 115020. [\[CrossRef\]](#)
9. Machala, Z.; Chládeková, L.; Pelach, M. Plasma Agents in Bio-Decontamination by Dc Discharges in Atmospheric Air. *J. Phys. D Appl. Phys.* **2010**, *43*, 222001. [\[CrossRef\]](#)
10. Janda, M.; Martišovitéš, V.; Hensel, K.; Machala, Z. Generation of Antimicrobial Nox by Atmospheric Air Transient Spark Discharge. *Plasma Chem. Plasma Process.* **2016**, *36*, 767–781. [\[CrossRef\]](#)
11. Bruggeman, P.J.; Kushner, M.J.; Locke, B.R.; Gardeniers, J.G.E.; Graham, W.G.; Graves, D.B.; Hofman-Caris, R.C.H.M.; Maric, D.; Reid, J.P.; Ceriani, E.; et al. Plasmaliquid Interactions: A Review and Roadmap. *Plasma Sources Sci. Technol.* **2016**, *25*, 053002. [\[CrossRef\]](#)
12. Puač, N.; Gherardi, M.; Shiratani, M. Plasma Agriculture: A Rapidly Emerging Field. *Plasma Process. Polym.* **2018**, *15*, 1700174. [\[CrossRef\]](#)
13. Thirumdas, R.; Kothakota, A.; Annapure, U.; Siliveru, K.; Blundell, R.; Gatt, R.; Valdramidis, V.P. Plasma Activated Water (PAW): Chemistry, Physico-Chemical Properties, Applications in Food and Agriculture. *Trends Food Sci. Technol.* **2018**, *77*, 21–31. [\[CrossRef\]](#)

14. Brisset, J.-L.; Pawlat, J. Chemical Effects of Air Plasma Species on Aqueous Solutes in Direct and Delayed Exposure Modes: Discharge, Post-Discharge and Plasma Activated Water. *Plasma Chem. Plasma Process.* **2016**, *36*, 355–381. [[CrossRef](#)]
15. Machala, Z.; Tarabová, B.; Sersenová, D.; Janda, M.; Hensel, K. Chemical and Antibacterial Effects of Plasma Activated Water: Correlation with Gaseous and Aqueous Reactive Oxygen and Nitrogen Species, Plasma Sources and Air Flow Conditions. *J. Phys. D Appl. Phys.* **2018**, *52*, 034002. [[CrossRef](#)]
16. Kaushik, N.; Ghimire, B.; Li, Y.; Adhikari, M.; Veerana, M.; Kaushik, N.; Jha, N.; Adhikari, B.; Lee, S.-J.; Masur, K.; et al. Biological and Medical Applications of Plasma-Activated Media, Water and Solutions. *Biol. Chem.* **2018**, *400*, 39–62. [[CrossRef](#)] [[PubMed](#)]
17. Lu, P.; Boehm, D.; Bourke, P.; Cullen, P.J. Achieving Reactive Species Specificity Within Plasma-Activated Water Through Selective Generation Using Air Spark and Glow Discharges. *Plasma Process. Polym.* **2017**, *14*, 1600207. [[CrossRef](#)]
18. Lukes, P.; Locke, B.R.; Brisset, J.-L. Aqueous-phase chemistry of electrical discharge plasma in water and in gas–liquid environments. In *Plasma Chemistry and Catalysis in Gases and Liquids*; Wiley-VCH Verlag & Co. KGaA: Weinheim, Germany, 2012; pp. 243–308. ISBN 978-3-527-64952-5.
19. Lukes, P.; Dolezalova, E.; Sisrova, I.; Clupek, M. Aqueous-Phase Chemistry and Bactericidal Effects from an Air Discharge Plasma in Contact with Water: Evidence for the Formation of Peroxynitrite Through a Pseudo-Second-Order Post-Discharge Reaction of H₂O₂ and HNO₂. *Plasma Sources Sci. Technol.* **2014**, *23*, 015019. [[CrossRef](#)]
20. Huang, D.M.; Chen, Z.M. Reinvestigation of the Henry's Law Constant for Hydrogen Peroxide with Temperature and Acidity Variation. *J. Environ. Sci.* **2010**, *22*, 570–574. [[CrossRef](#)]
21. Kruszelnicki, J.; Lietz, A.M.; Kushner, M.J. Atmospheric Pressure Plasma Activation of Water Droplets. *J. Phys. D Appl. Phys.* **2019**, *52*, 355207. [[CrossRef](#)]
22. Hassan, M.E.; Janda, M.; Machala, Z. Transport of Gaseous Hydrogen Peroxide and Ozone into Bulk Water vs. Electrospayed Aerosol. *Water* **2021**, *13*, 182. [[CrossRef](#)]
23. Stratton, G.R.; Bellona, C.L.; Dai, F.; Holsen, T.M.; Thagard, S.M. Plasma-Based Water Treatment: Conception and Application of a New General Principle for Reactor Design. *Chem. Eng. J.* **2015**, *273*, 543–550. [[CrossRef](#)]
24. Zeleny, J. The Electrical Discharge from Liquid Points, and a Hydrostatic Method of Measuring the Electric Intensity at Their Surfaces. *Phys. Rev.* **1914**, *3*, 69–91. [[CrossRef](#)]
25. Zeleny, J. Instability of Electrified Liquid Surfaces. *Phys. Rev.* **1917**, *10*, 1–6. [[CrossRef](#)]
26. Dwivedi, P.; Matz, L.M.; Atkinson, D.A.; Hill, H.H., Jr. Electro spray ionization-ion mobility spectrometry: A rapid analytical method for aqueous nitrate and nitrite analysis. *Analyst* **2004**, *129*, 139–144. [[CrossRef](#)]
27. Jaworek, A. Electro spray droplet sources for thin film deposition. *J. Mater. Sci.* **2007**, *42*, 266–297. [[CrossRef](#)]
28. Carotenuto, C.; Di Natale, F.; Lancia, A. Wet Electrostatic Scrubbers for the Abatement of Submicronic Particulate. *Chem. Eng. J.* **2010**, *165*, 35–45. [[CrossRef](#)]
29. Cui, H.; Li, N.; Peng, J.; Cheng, J.; Zhang, N.; Wu, Z. Modeling the Particle Scavenging and Thermal Efficiencies of a Heat Absorbing Scrubber. *Build. Environ.* **2017**, *111*, 218–227. [[CrossRef](#)]
30. Jaworek, A.; Sobczyk, A.T.; Krupa, A. Electro spray Application to Powder Production and Surface Coating. *J. Aerosol Sci.* **2018**, *125*, 57–92. [[CrossRef](#)]
31. Boda, S.K.; Li, X.; Xie, J. Electro spraying an Enabling Technology for Pharmaceutical and Biomedical Applications: A Review. *J. Aerosol Sci.* **2018**, *125*, 164–181. [[CrossRef](#)]
32. Ball, A.K.; Roy, S.S.; Kisku, D.R.; Murmu, N.C.; Dos Santos Coelho, L. Optimization of Drop Ejection Frequency in EHD Inkjet Printing System Using an Improved Firefly Algorithm. *Appl. Soft Comput.* **2020**, *94*, 106438. [[CrossRef](#)]
33. Kim, S.; Jung, M.; Choi, S.; Lee, J.; Lim, J.; Kim, M. Discharge Current of Water Electro spray with Electrical Conductivity under High-Voltage and High-Flow-Rate Conditions. *Exp. Therm. Fluid Sci.* **2020**, *118*, 110151. [[CrossRef](#)]
34. Kim, Y.; Jung, S.; Kim, S.; Choi, S.T.; Kim, M.; Lee, H. Heat Transfer Performance of Water-Based Electro spray Cooling. *Int. Commun. Heat Mass Transf.* **2020**, *118*, 104861. [[CrossRef](#)]
35. Borra, J.-P. Review on Water Electro-Sprays and Applications of Charged Drops with Focus on the Corona-Assisted Cone-Jet Mode for High Efficiency Air Filtration by Wet Electro-Scrubbing of Aerosols. *J. Aerosol Sci.* **2018**, *125*, 208–236. [[CrossRef](#)]
36. Rosell-Llompart, J.; Grifoll, J.; Loscertales, I.G. Electro sprays in the Cone-Jet Mode: From Taylor Cone Formation to Spray Development. *J. Aerosol Sci.* **2018**, *125*, 2–31. [[CrossRef](#)]
37. Jaworek, A.; Gañán-Calvo, A.M.; Machala, Z. Low Temperature Plasmas and Electro sprays. *J. Phys. D Appl. Phys.* **2019**, *52*, 233001. [[CrossRef](#)]
38. Kanev, I.L.; Mikheev, A.Y.; Shlyapnikov, Y.M.; Shlyapnikova, E.A.; Morozova, T.Y.; Morozov, V.N. Are Reactive Oxygen Species Generated in Electro spray at Low Currents? *Anal. Chem.* **2014**, *86*, 1511–1517. [[CrossRef](#)] [[PubMed](#)]
39. Burlica, R.; Grim, R.G.; Shih, K.-Y.; Balkwill, D.; Locke, B.R. Bacteria Inactivation Using Low Power Pulsed Gliding Arc Discharges with Water Spray. *Plasma Process. Polym.* **2010**, *7*, 640–649. [[CrossRef](#)]
40. Oinuma, G.; Nayak, G.; Du, Y.; Bruggeman, P.J. Controlled Plasmadroplet Interactions: A Quantitative Study of OH Transfer in Plasmaliquid Interaction. *Plasma Sources Sci. Technol.* **2020**, *29*, 095002. [[CrossRef](#)]
41. Kovalova, Z.; Leroy, M.; Kirkpatrick, M.J.; Odic, E.; Machala, Z. Corona Discharges with Water Electro spray for *Escherichia coli* Biofilm Eradication on a Surface. *Bioelectrochemistry* **2016**, *112*, 91–99. [[CrossRef](#)]
42. Becker, K.; Kleffmann, J.; Kurtenbach, A.; Wiesen, P. Solubility of Nitrous Acid (HONO) in Sulfuric Acid Solutions. *J. Phys. Chem.* **1996**, *100*, 14984–14990. [[CrossRef](#)]

43. Lee, Y.N.; Schwartz, S.E. Reaction Kinetics of Nitrogen Dioxide with Liquid Water at Low Partial Pressure. *J. Phys. Chem.* **1981**, *85*, 840–848. [[CrossRef](#)]
44. Armor, J.N. Influence of pH and Ionic Strength Upon Solubility of Nitric Oxide in Aqueous Solution. *J. Chem. Eng. Data* **1974**, *19*, 82–84. [[CrossRef](#)]
45. Kučerová, K.; Machala, Z.; Hensel, K. Transient Spark Discharge Generated in Various N₂/O₂ Gas Mixtures: Reactive Species in the Gas and Water and Their Antibacterial Effects. *Plasma Chem. Plasma Process.* **2020**, *40*, 749–773. [[CrossRef](#)]
46. Janda, M.; Martišovits, V.; Machala, Z. Transient Spark: A Dc-Driven Repetitively Pulsed Discharge and Its Control by Electric Circuit Parameters. *Plasma Sources Sci. Technol.* **2011**, *20*, 035015. [[CrossRef](#)]
47. Janda, M.; Machala, Z.; Niklová, A.; Martišovits, V. The Streamer-to-Spark Transition in a Transient Spark: A Dc-Driven Nanosecond-Pulsed Discharge in Atmospheric Air. *Plasma Sources Sci. Technol.* **2012**, *21*, 045006. [[CrossRef](#)]
48. Gordon, I.E.; Rothman, L.S.; Hill, C.; Kochanov, R.V.; Tan, Y.; Bernath, P.F.; Birk, M.; Boudon, V.; Campargue, A.; Chance, K.V.; et al. The HITRAN2016 Molecular Spectroscopic Database. *J. Quant. Spectrosc. Radiat. Transf.* **2017**, *203*, 3–69. [[CrossRef](#)]
49. Kochanov, R.V.; Gordon, I.E.; Rothman, L.S.; Shine, K.P.; Sharpe, S.W.; Johnson, T.J.; Wallington, T.J.; Harrison, J.J.; Bernath, P.F.; Birk, M.; et al. Infrared Absorption Cross-Sections in HITRAN2016 and Beyond: Expansion for Climate, Environment, and Atmospheric Applications. *J. Quant. Spectrosc. Radiat. Transf.* **2019**, *230*, 172–221. [[CrossRef](#)]
50. Keller-Rudek, H.; Moortgat, G.K.; Sander, R.; Sörensen, R. The MPI-Mainz UV/VIS Spectral Atlas of Gaseous Molecules of Atmospheric Interest. *Earth Syst. Sci. Data* **2013**, *5*, 365–373. [[CrossRef](#)]
51. Oehmigen, K.; Hähnel, M.; Brandenburg, R.; Wilke, C.; Weltmann, K.-D.; Von Woedtke, T. The Role of Acidification for Antimicrobial Activity of Atmospheric Pressure Plasma in Liquids. *Plasma Process. Polym.* **2010**, *7*, 250–257. [[CrossRef](#)]
52. Chauvin, J.; Judée, F.; Yousfi, M.; Vicendo, P.; Merbahi, N. Analysis of Reactive Oxygen and Nitrogen Species Generated in Three Liquid Media by Low Temperature Helium Plasma Jet. *Sci. Rep.* **2017**, *7*, 4562. [[CrossRef](#)] [[PubMed](#)]
53. Anderson, C.E.; Cha, N.R.; Lindsay, A.D.; Clark, D.S.; Graves, D.B. The Role of Interfacial Reactions in Determining Plasma–Liquid Chemistry. *Plasma Chem. Plasma Process.* **2016**, *36*, 1393–1415. [[CrossRef](#)]
54. Wende, K.; Williams, P.; Dalluge, J.; Gaens, W.V.; Aboubakr, H.; Bischof, J.; Von Woedtke, T.; Goyal, S.M.; Weltmann, K.D.; Bogaerts, A.; et al. Identification of the biologically active liquid chemistry induced by a nonthermal atmospheric pressure plasma jet. *Biointerphases* **2015**, *10*, 029518. [[CrossRef](#)]
55. Tian, Y.; Ma, R.; Zhang, Q.; Feng, H.; Liang, Y.; Zhang, J.; Fang, J. Assessment of the Physicochemical Properties and Biological Effects of Water Activated by Non-Thermal Plasma above and Beneath the Water Surface. *Plasma Process. Polym.* **2015**, *12*, 439–449. [[CrossRef](#)]
56. Lu, P.; Boehm, D.; Cullen, P.; Bourke, P. Controlled Cytotoxicity of Plasma Treated Water Formulated by Open-Air Hybrid Mode Discharge. *Appl. Phys. Lett.* **2017**, *110*, 264102. [[CrossRef](#)]
57. Kovačević, V.V.; Dojčinović, B.P.; Jović, M.; Roglič, G.M.; Obradović, B.M.; Kuraica, M.M. Measurement of Reactive Species Generated by Dielectric Barrier Discharge in Direct Contact with Water in Different Atmospheres. *J. Phys. D Appl. Phys.* **2017**, *50*, 155205. [[CrossRef](#)]
58. Tarabová, B.; Lukeš, P.; Janda, M.; Hensel, K.; Šikurová, L.; Machala, Z. Specificity of Detection Methods of Nitrites and Ozone in Aqueous Solutions Activated by Air Plasma. *Plasma Process. Polym.* **2018**, *15*, 1800030. [[CrossRef](#)]
59. Eisenberg, G. Colorimetric Determination of Hydrogen Peroxide. *Ind. Eng. Chem. Anal. Ed.* **1943**, *15*, 327–328. [[CrossRef](#)]
60. Janda, M.; Machala, Z.; Lacoste, D.; Stancu, G.D.; Laux, C.O. Stabilization of A Lean Methane-Air Flame Using Transient Spark Discharge. In Proceedings of the 13th International Symposium on High Pressure Low Temperature Plasma Chemistry (Hakone XIII), Kazimierz Dolny, Poland, 9–14 September 2012; pp. 185–189.
61. Borra, J.-P.; Ehouarn, P.; Boulaud, D. Electrohydrodynamic Atomisation of Water Stabilised by Glow Discharge—Operating Range and Droplet Properties. *J. Aerosol Sci.* **2004**, *35*, 1313–1332. [[CrossRef](#)]
62. Janda, M.; Hensel, K.; Machala, Z. Chemical Kinetic Model of Transient Spark: Spark Phase and NO_x Formation. In Proceedings of the 22nd Symposium on Applications of Plasma Processes and 11th Eu-Japan Joint Symposium on Plasma Processing Sapp XXII, Strbske Pleso, Slovakia, 18–24 January 2019; pp. 25–32.
63. Capitelli, M.; Ferreira, C.M.; Gordiets, B.F.; Osipov, A.I. *Plasma Kinetics in Atmospheric Gases*; Springer: Berlin/Heidelberg, Germany, 2000.
64. Janda, M.; Martišovits, V.; Hensel, K.; Dvonč, L.; Machala, Z. Measurement of the Electron Density in Transient Spark Discharge. *Plasma Sources Sci. Technol.* **2014**, *23*, 065016. [[CrossRef](#)]
65. Herron, J. Evaluated Chemical Kinetics Data for Reactions of N(²D), N(²P), and N₂(A³Σ_u⁺) in the Gas Phase. *J. Phys. Chem. Ref. Data* **1999**, *28*, 1453–1483. [[CrossRef](#)]
66. Melton, C.E. Cross Sections and Interpretation of Dissociative Attachment Reactions Producing OH⁻, O⁻, and H⁻ in H₂O. *J. Chem. Phys.* **1972**, *57*, 4218–4225. [[CrossRef](#)]
67. Lowke, J.J.; Morrow, R. Theoretical analysis of removal of oxides of sulphur and nitrogen in pulsed operation of electrostatic precipitators. *IEEE Trans. Plasma Sci.* **1995**, *23*, 661–671. [[CrossRef](#)]